Microstructural design by combining nanograins and spinodal decomposition in a Fe-Cr alloy

Juan Macchi, Olha Nakonechna, Ronan Henry, Celia Castro, Kaveh Edalati, Frederic de Geuser, Xavier Sauvage, Williams Lefebvre

Scripta Materialia 252 (2024) 116247

Contents lists available at ScienceDirect

Scripta Materialia

journal homepage: www.journals.elsevier.com/scripta-materialia

Microstructural design by combining nanograins and spinodal decomposition in a Fe-Cr alloy

Juan Macchi [a,*], Olha Nakonechna [a], Ronan Henry [a], Celia Castro [a], Kaveh Edalati [b], Frederic De Geuser [c], Xavier Sauvage [a], Williams Lefebvre [a]

[a] Univ Rouen Normandie, INSA Rouen Normandie, CNRS, Normandie Univ, GPM UMR 6634, F-76000 Rouen, France
[b] WPI, International Institute for Carbon-Neutral Energy Research (WPI-I2CNER), Kyushu University, Fukuoka, Japan
[c] University Grenoble Alpes, CNRS, Grenoble INP, SIMaP, Grenoble F-38000, France

ARTICLE INFO

Keywords:
Spinodal decomposition
HPT
APT
Fracture toughness
Micro-cantilever

ABSTRACT

Microstructure design of new high-performance alloys requires the combination of multiple hardening mechanisms. This study explores combining nanograins with spinodal decomposition strengthening in an Fe-51.4Cr (at. %) alloy. High-pressure torsion (HPT) produced a nanostructure with a 51 nm grain size. Atom probe tomography analysis of deformed and annealed samples revealed spinodal decomposition after one hour of annealing. HPT accelerated decomposition kinetics is due to the high vacancy concentration. Microhardness remained stable due to spinodal hardening, despite a decrease in the Hall-Petch strengthening contribution. However, fracture toughness decreased.

The necessity of reducing carbon dioxide emissions in the transportation industry has led to an increasing requirement for alloys exhibiting enhanced properties and performances. In order to achieve an enhanced yield strength, microstructural design represents a pivotal tool in this process. The microstructures of the materials are therefore designed to produce high hardening in each dislocation-stopping mechanism (such as solid solution, dislocation forest, second phases, grain boundaries [1,2]) or to achieve the best balance between them [3–5].

Metallic nanostructures, produced by sputter deposition or severe plastic deformation (SPD), exhibit high strengthening by the Hall-Petch effect when the grain size is in the order of tens of nanometers up to hundreds of nanometers [4,5]. The nanostructured materials, with a high grain boundary density, may facilitate heterogeneous precipitation [6,7], which has the effect of disfavoring hardening. This is due to the fact that ineffective precipitation and the removal of solid solution elements occur. Moreover, the accelerated kinetics of the precipitation process renders precipitation hardening unstable at elevated temperatures [7].

In the present study, an additional non-precipitation hardening mechanism is pursued in addition to a high Hall-Petch hardening to enhance the mechanical properties. It has been demonstrated that spinodal decomposition can act as a hardening mechanism [8]. According to the elastic field theory, the lattice misfit and the modulus difference are the causes of this hardening [9]. Spinodal decomposition occurs spontaneously, without the need for a thermodynamic barrier, and without the involvement of a classical nucleation mechanism. As a consequence, this hardening mechanism might be less negatively affected by the nanostructure than the precipitation hardening. Finally, the nanograin structure combined with the spinodal decomposition hardening could result in an effective increase of the effective mechanical properties and, therefore, in the structure lightening.

However, previous studies have not demonstrated a positive interaction between spinodal decomposition and nanostructures. For instance, grain boundary segregation impeded decomposition in a Pt-Au system [10], while "Schwarz crystals" were proposed to impede decomposition in an Al-Zn alloy [11].

The Fe-Cr system is a promising candidate due to its large miscibility gap, which is conducive to spinodal decomposition, and its well-established nuclear applications.

To explore the possibility of simultaneous strengthening by Hall-Petch and spinodal decomposition, a Fe-51.4Cr (at.%) alloy was chosen. This material was previously studied [12] in a coarse-grained state with long annealing. Those states serve as reference here. To investigate the interaction between spinodal decomposition and a nanostructure, SPD via high-pressure torsion (HPT) was applied prior to aging heat

* Corresponding author at: GPM, Avenue de l'Université, 76800 Saint-Étienne-du-Rouvray, France.
E-mail address: juan.macchi@univ-rouen.fr (J. Macchi).

https://doi.org/10.1016/j.scriptamat.2024.116247
Received 19 March 2024; Received in revised form 5 June 2024; Accepted 21 June 2024
Available online 6 July 2024

treatments at 525 °C for varying durations.

The HPT process was conducted at a pressure of 6 GPa with a deformation rate of 1 revolution per minute and a total of 10 revolutions at room temperature. The grain size in the obtained samples was characterized using transmission Kikuchi diffraction (TKD) in a Helios 5UX microscope and an Oxford Symmetry EBSD detector (30 kV, WD set to 6.5 mm). The obtained data were processed using the AZtecCrystal MapSweeper software (16 × 16 binning for indexing and refining).

The nanostructure of the deformed sample without aging (designated in the following as the HPT state) is presented in Fig. 1.a. Fig. 1.b shows the ultrafine structure of an HPT sample aged at 525 °C. After 100 h, a clear growth in the structure size was observed, transitioning from a nanostructure state (below 100 nm) to an ultrafine grain regime (larger than 100 nm). The analysis of 2296 and 483 grains (minimum disorientation set to 10°, minimum grain surface area 50 nm^2) for the HPT and HPT-100 h conditions, respectively, yielded the probability density distributions shown in Fig. 1.c. The mean size of the HPT-100 h sample (159 nm) is approximately three times higher than the mean size of the HPT sample (51 nm). These values are in good agreement with those reported in [20,21].

Atom probe tomography (APT) was employed to ascertain the local compositions at different stages. A LEAP® 5000 XS instrument was employed with the following settings: impulse rate of 500 kHz, detection rate of 0.5 %, pulse fraction of 0.2 %, and temperature of 50 K. The samples were reconstructed in 3D using the IVAS® suite, followed by data processing with Gpm_3dSAT software (IDDN.FR.001.430017.000.S.P.2020.000.10000).

Both the solution heat-treated (SHT) sample and the HPT sample (Fig. 2.a) exhibit a homogeneous composition, with Cr atoms appearing green). Notably, a grain boundary is visible in the HPT sample, identified by a change in the density poles (detailed in Appendix A), with no segregation. The HPT-100 h sample, however, exhibits a heterogeneous distribution of Cr ions with a spinodal-like morphology within the grains (highlighted by the red area in Fig. 2.b). No evidence of sigma phase precipitation was observed in any of the sample.

The non-aged HPT samples did not exhibit grain boundary segregation or phase decomposition. The profile analysis of the region of interest (ROI) in black (Fig. 2.a), presented in Fig. 2.c, did not reveal any evidence of grain boundary segregation. The HPT-100 h sample shows grain boundary segregation, as illustrated in Fig. 2.c. Despite this segregation, the mean composition of the in-grain ROI, as shown in Fig. 2.b, is comparable to that of the alloy, indicating no clear depletion of Cr in that grain. However, a depleted region is observed in close proximity to the grain boundary.

To assess the kinetics of spinodal decomposition at 525 °C in the nanograin microstructure, the Radial Distribution Function (RDF)

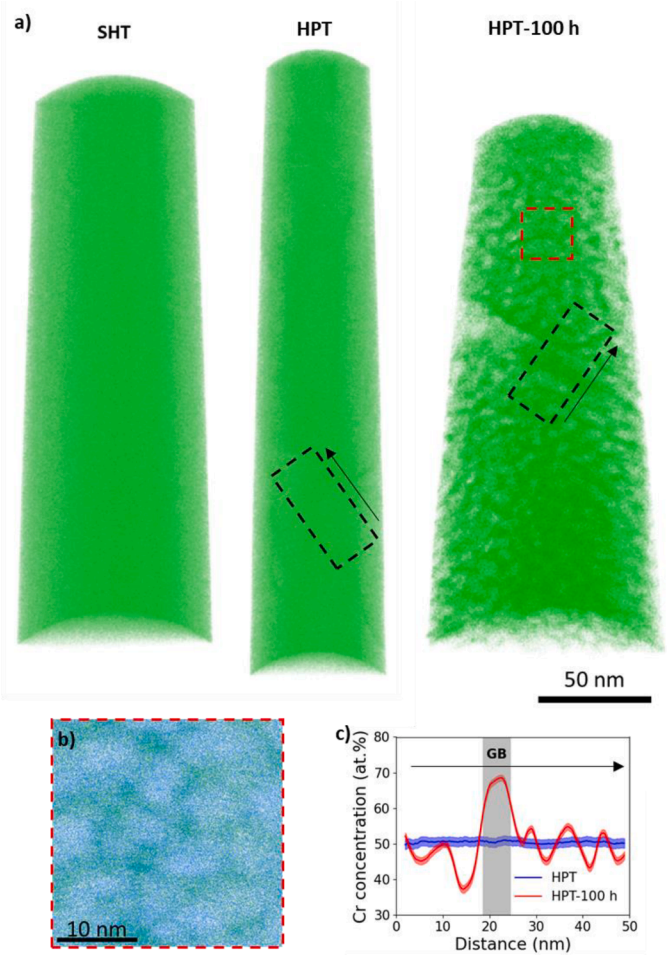

Fig. 2. a) 3D reconstructions of an annealed sample (SHT) prior to HPT, annealed plus 10 revolutions (HPT), and annealed plus 10 revolutions HPT and aged 100 h at 525 °C (HPT-100 h); in green 5 % of Cr ions are shown. b) A ROI selected in the interior of a grain of the HPT-100 h condition (in green Cr ions, in blue Fe ions). c) Cr concentration profiles across a grain boundary for the HPT and the HPT-100 h conditions.

[13–15] was applied to APT datasets (Fig. 3.a). This approach enables the measurement of both the amplitude and the wavelength of the composition fluctuations are accessible. After aging, the initiation of spinodal decomposition is revealed. Although only one sample exhibited

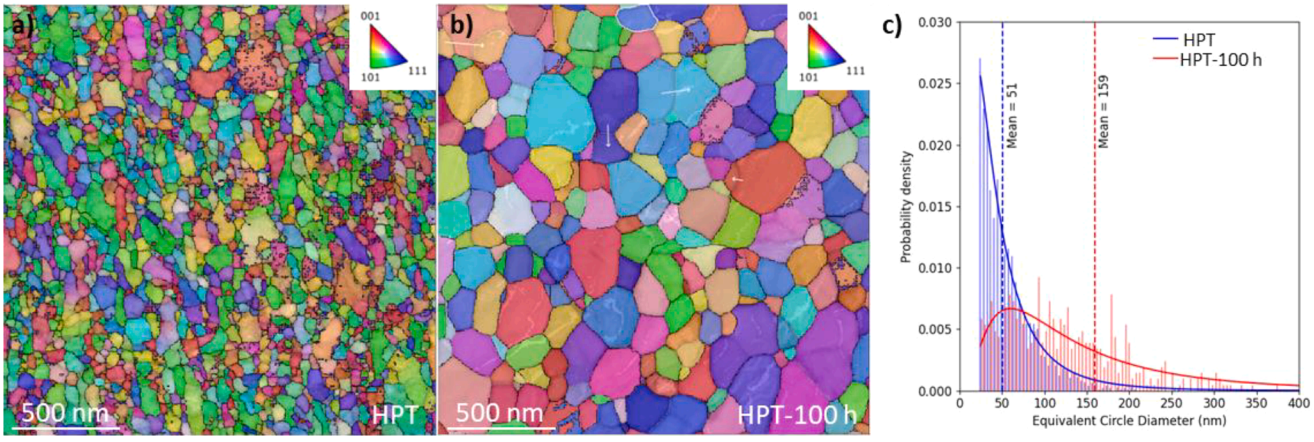

Fig. 1. a) Inverse Pole Figure (IPF) map of the HPT sample. b) IPF map of the HPT sample aged 100 h at 525 °C. c) Probability density of the equivalent circle diameter grain size as well as the mean value, for the conditions presented in a) and b).

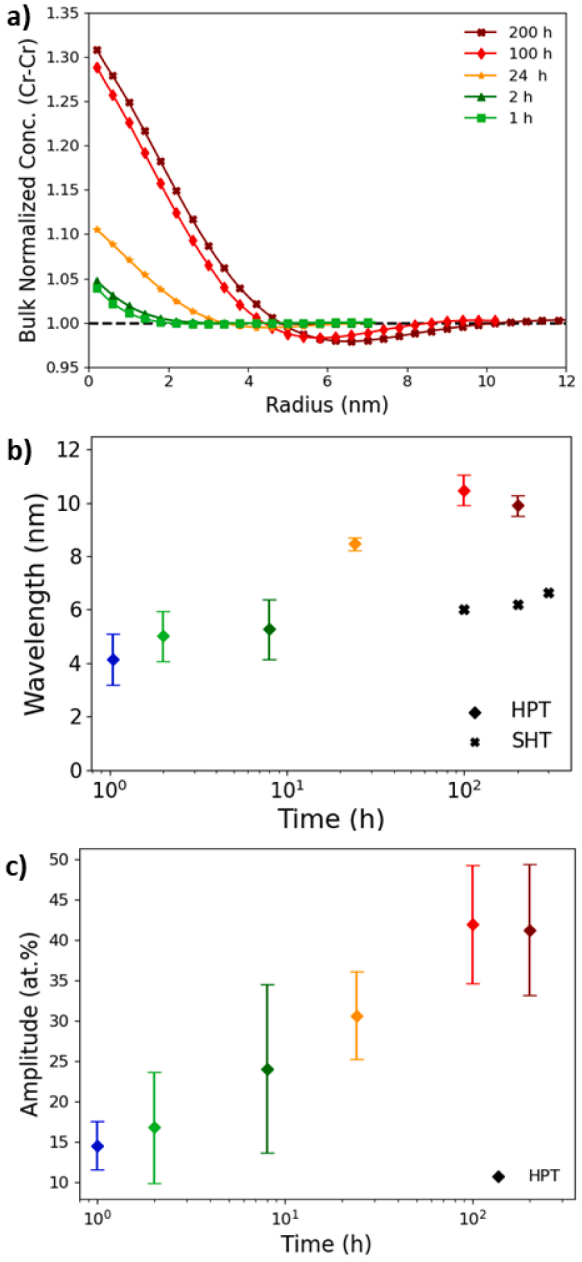

Fig. 3. a) Radial distribution functions (RDF) of the HPT samples after different holding times at 525 °C. b) Wavelength for the HPT and for the non-deformed samples. c) Amplitude between the Cr-enriched and Cr-depleted regions by the methods presented in [13,15].

a clear minimum in its RDF (related to depleted zones in long-range order) after one hour of holding, minima were evident for all other holding times, as illustrated in Fig. 3.a. The minimum value decreased with longer heat treatments, and its position shifted towards higher radii as previously reported for spinodal decomposition progress in [12,13].

The quantitative analysis of the spinodal decomposition can be addressed by analyzing the RDFs using various methods, as reported in [12–17]. In the present study the wavelength is obtained by fitting the RDF with an appropriate equation (a detailed explanation is presented in Appendix B). In [12], the wavelength was identified as the double of the distance to the minimum of the RDF.

Fig. 3.b presents the evolution of the wavelength with the aging time. A rapid increase in the wavelength is revealed at the onset of composition fluctuations (up to 2 h), followed by a rapid kinetics between 2 h and 100 h. Finally, a slower kinetics section is observed. The non-deformed samples present smaller values of spinodal wavelength as well as a smaller slope, indicating slower kinetics.

The amplitude of the spinodal decomposition was determined by the methodology presented in Appendix B, considering a one-dimensional sinusoidal profile ($\Lambda = \sqrt{2}$), which yielded to the results shown in Fig. 3.c. The fast increase followed by stagnation is expected for spinodal fluctuations, which then give rise to by the coarsening of fully developed hills and valleys. The amplitude observed during the stagnation period (from 100 h) is comparable with the thermodynamic values expected from a total decomposition if Λ is equal to 2. In this case, our experimental amplitude is 59 at.% which is in accordance with the calculations obtained from ThermoCalc [18], thermodynamic database TCFE8 (62 at.%).

After SPD, the spinodal decomposition quantified in Fig. 2 and 3 presents faster kinetics, resulting in a larger and fast-growing wavelength and in an amplitude that is fully developed after 100 h. Despite the difficulty in making comparisons with the literature due to differences in Cr compositions and aging temperatures, the amplitude value of the SPD sample after 100 h is significantly higher than in other studies without SPD processing [19–21]. In the aforementioned references, a similar amplitude is only reached after 1000 h to 2000 h. In [12], after 552 h at 525 °C (the same alloy as the one under investigation in the present study), a 56.6 at.% Cr amplitude was reached (as established using the method of [13]). At the same temperature, the same amplitude was already obtained after only 100 h of holding in the HPT samples.

The accelerated kinetics can be attributed to a faster diffusion which is anticipated from the Cahn-Hilliard equations and their dependence on the mobility [22]. The diffusion of substitutional atoms is directly correlated with the number density of vacancies. In the case of SPD samples, the fraction of non-equilibrium vacancies has been estimated to be between 1×10^{-5} and 5×10^{-4} [23–26] which are several orders of magnitude higher than the thermal-equilibrium vacancy fraction (10^{-13} at 600 °C) [27].

The fraction of non-equilibrium vacancies would evolve during the aging heat treatment reaching the equilibrium if the holding time is sufficiently long. At a given temperature, the evolution of the diffusion coefficient as a function of the time, depending on the vacancy fraction, can be expressed as follows [27]:

$$D(t) = D_E + (D_0 - D_E)\frac{\tau}{t}\ln\left(1+\frac{t}{\tau}\right) \quad (1)$$

where τ is the time constant of annihilation (set at 238 s [27]), t is the time. The annihilation time is considered constant as a first approximation (annihilation would be overestimated), even though the grain size evolves. D_0 represents the initial diffusivity at $t = 0$ while D_E denotes the diffusivity at the equilibrium state, which is reached once all excess vacancies have been annihilated. In both cases, the diffusivity can be calculated as follows:

$$D_i = c_i a^2 \nu \exp\left(\frac{\Delta S}{k_B}\right)\exp\left(\frac{-\Delta H}{k_B T}\right) \quad (2)$$

where c_i is the vacancy fraction at $t = 0$ and at the thermal equilibrium, a is the jump length ($a = 0.25$ nm), ν is the Debye frequency ($\nu \approx 10^{-13}$ s^{-1}), $\Delta S \approx 5\ k_B$ is the entropy change during Fe diffusion [28], ΔH is the migration activation enthalpy of Fe vacancies (0.8 eV [27]), k_B is the Boltzmann constant and T is the absolute temperature.

For the purposes of this analysis, a vacancy fraction of 1 × 10–12 is considered to be the upper limit for the thermal equilibrium state. This value is based on the observation that vacancy fractions in Fe at 525 °C [29], and in Fe-Cr alloys with higher formation enthalpies [30]. After the HPT deformation process, vacancy fractions of approximately 1.35×10^{-5} have been reported in pure Fe [31], while in other metals, vacancy fractions have been measured to be close to 1×10^{-4} [24]. In ECAP samples, the vacancy concentration was calculated to be between 5×10^{-4} and 5×10^{-3} [32]. However, a lower value of 1×10^{-6} was set due

to the higher mobility of Cr. According to Eqs. (1) and 2 and considering the aforementioned vacancy fractions, the diffusion coefficient varies as presented in Fig. 4.

As illustrated in Fig. 4, the diffusion coefficient at the outset of the annealing heat treatment is consistent with the predicted value based on the excess vacancy concentration (8×10^{-14} m^2/s) while it decreases with the holding time. However, with the progression of holding time, the diffusion coefficient exhibits a decline. The times corresponding to the studied holding conditions (1, 2, 8, 24, 100, and 200 h) are indicated by vertical lines. After 1 h, the diffusion coefficient is calculated equal to be 1.5×10^{-14} m^2/s, while it drops to 2.1×10^{-16} m^2/s after 200 h. Despite a drop of two orders of magnitude is determined, the diffusivity after 200 h in the HPT is still expected to be 5 orders of magnitude higher than the value expected only by the presence of thermal vacancies at equilibrium (8.2×10^{-23} m^2/s). Although the annihilation of vacancies is expected to occur more rapidly in SPD samples, the difference in diffusion coefficients between Fe and Cr may result in the dynamic generation of vacancies via a Kirkendall effect [33].

The spinodal decomposition can be modeled by calculating the evolution of the Gibbs energy as presented by the Cahn & Hilliard analysis in isobarothermal condition [22]. The Fe mobility is comparable to that of Cr and to the interdiffusion ones (up to 75 at.% Cr) [34–36]. As the flux of Fe is directly proportional to the diffusion coefficient, the rate of evolution of the microstructure is related to the diffusion coefficient. It is therefore anticipated that a higher vacancy concentration will result in faster kinetics at a given temperature where spinodal decomposition is expected. The slower section of the wavelength evolution can be then related to slower diffusion as well as to the coarsening mechanism.

This study investigated the effect of spinodal decomposition on the mechanical behavior of a nanocrystalline alloy. In the non-deformed sample (Fig. 5.a), annealing resulted in increased hardness due to spinodal decomposition. The initial hardness of the HPT sample was 500 HV higher than that of the bulk alloy due to its smaller grain size, which corresponded to a Hall-Petch constant of 340 $MPa.\mu m^{-0.5}$ (by considering the Tabor's relationship between hardness and yield strength [37]).

The HPT states exhibited a slight initial decline in hardness (70 HV) followed by period of stability up to 100 h of annealing. Between 100 and 200 h, a final decrease was observed. Despite a threefold increase in grain size after 200 h, hardness only decreased by 100 HV. This indicates that spinodal decomposition partially offsets the hardness loss resulting from grain growth (652 MPa, approximately 220 HV). The strengthening mechanism of spinodal decomposition is attributed to the interaction between dislocations and the difference in elastic moduli, and the lattice misfit, as predicted by elastic field theory [9].

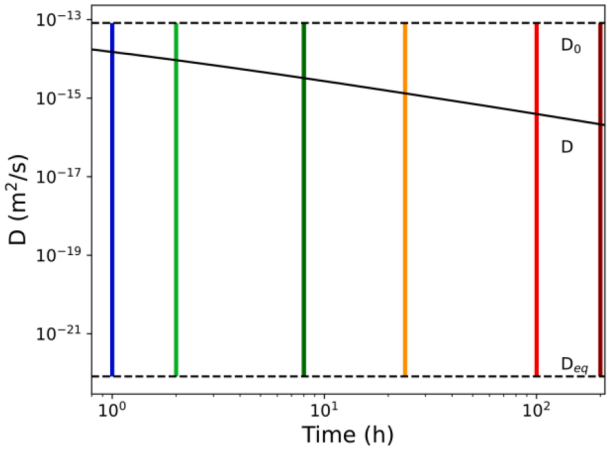

Fig. 4. Evolution of the diffusion coefficient (D) during an annealing heat treatment at 525 °C, showing the value produced by the equilibrium thermal vacancies' concentration (D_{eq}) and the diffusion coefficient due to the concentration of excess vacancies produced by the HPT process (D_0). Vertical lines show the times at which APT analysis has been performed (1, 2, 8, 24, 100 and 200 h).

It is noteworthy that the hardness difference between the HPT-100 h and non-deformed 100 h samples (300 HV, or 900 MPa) can be largely explained by the Hall-Petch effect ($340/\sqrt{0.159}$ MPa).

In addition to hardness evolution, the fracture toughness K_{IC} was measured in selected conditions. This measurement was conducted by subjecting pre-notched microcantilevers with a square surface area of approximately 3×5 μm^2, a notch depth of 2 μm and a length of 20 μm to in-situ deformation. Details of the microcantilever fabrication, images and testing are presented in Appendix C. In order to compare the curves between tests, the stress intensity factor calculated under the linear elastic hypothesis (K_{LEFM}) of the HPT and HPT-100 h are presented in Fig. 5.b. The obtained curves demonstrate the presence of plasticity. After the elastic domain, there is no brittle fracture but rather a non-linearity relating to plasticity, which is then followed by crack propagation.

The resulting $K_{Q,J_{ini}}$ (calculated as presented in Appendix C) is equal to 10.4 ± 0.9 MPa $m^{1/2}$ for the HPT condition. This value is slightly smaller than the K_{IC} of ultrafine-grained (UFG) Fe [38,39] but it is higher than the one of UFG Cr [40] for a similar charging direction (a smaller grain size was measured in the present study). The $K_{Q,J_{ini}}$ of the HPT-100 h condition was calculated to be equal to 5.5 ± 1.0 MPa $m^{1/2}$.

It is not possible to determine the effect of spinodal decomposition on dislocation nucleation and storage (and the fracture toughness) by comparing the HPT and HPT-100 h conditions, due to the supplementary grain size difference between the two states.

The reduction in the fracture toughness may be attributed to diminished dislocation mobility resulting from the highly evolved spinodal decomposition, as documented in [41,42]. The reduced dislocation mobility has been corroborated by in situ compression TEM characterization [41]. The diminished dislocation mobility is partially attributed to the pinning effect of dislocations traversing Cr-Cr pairs, which intensifies with the spinodal decomposition [42]. Xin et al. demonstrated that the solute-rich/poor interphases may serve as nucleation sites for dislocations, resulting in a rapid accumulation of dislocations within the material [43].

In contrast to the suppression of the spinodal decomposition by the presence of nanocrystals in the Pt-Au [10] and Al-Zn [11] systems, the present study demonstrates the possibility of combining an UFG structure with a spinodal decomposition in a Fe-Cr alloy (51.4 at.% Cr). The developed microstructure exhibited significantly enhanced hardness compared to the non-deformed state, even after prolonged annealing at 525 °C. The high hardness is partially attributed to the nanocrystalline microstructure (51 nm), which transitions to an ultrafine regime (159 nm), and partially due to the spinodal decomposition hardening.

The kinetics of the spinodal decomposition within the grains of the nanostructured alloy were compared with those of the non-deformed conditions. The comparison revealed a larger wavelength for similar holding times as well as a higher amplitude in the case of the severely plastically deformed samples. Therefore, it can be concluded that the HPT process introduces a high vacancy concentration, and drastically accelerates the spinodal decomposition by a factor close to ten.

In the light of the present results and the observed stability of hardness upon annealing, it may be posited that the combination of a nanostructure with the spinodal decomposition may be pursued in the microstructure design, particularly in instances where the primary objective is the stabilization of high hardness. Furthermore, Fe-Cr alloys may also be considered as subjects of this new design path, along with others alloys with miscibility gaps, such as aluminum alloys (Al-Zn [44]) or bronzes (e.g. Cu-Ni-Sn [45]). However, due to the lower dislocation mobility following well-established spinodal decomposition, the annealing time may be adjusted to maintain high values of fracture

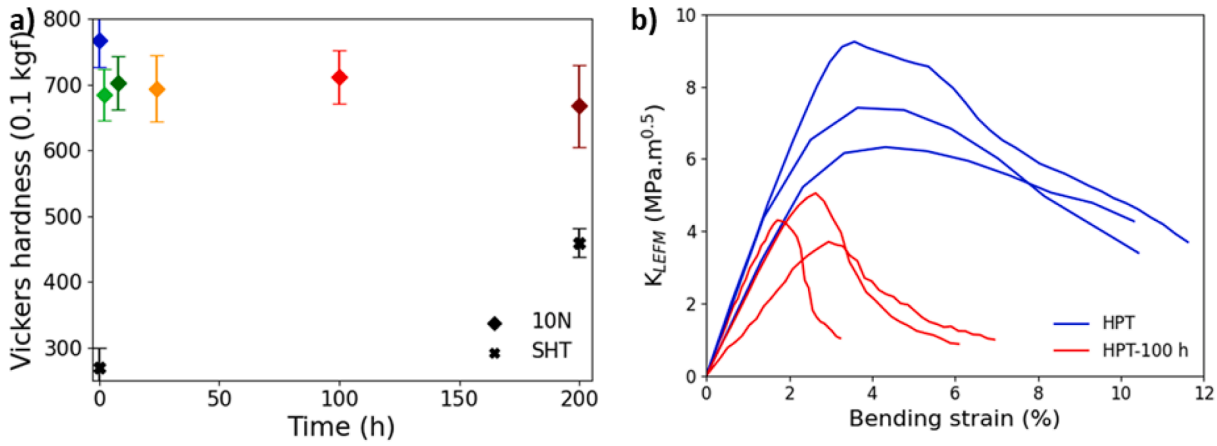

Fig. 5. a) Evolution of the microhardness after different holdings times at 525 °C of the non-deformed and HPT samples. b) Bending curves from HPT samples and HPT aged 100 h.

toughness.

CRediT authorship contribution statement

Juan Macchi: Writing – original draft, Methodology, Formal analysis, Data curation, Conceptualization. **Olha Nakonechna:** Methodology, Investigation. **Ronan Henry:** Writing – review & editing, Investigation, Formal analysis. **Celia Castro:** Writing – review & editing, Visualization. **Kaveh Edalati:** Writing – review & editing, Investigation. **Frederic De Geuser:** Writing – review & editing, Validation, Methodology. **Xavier Sauvage:** Writing – review & editing, Resources. **Williams Lefebvre:** Writing – original draft, Supervision, Project administration, Funding acquisition.

Declaration of competing interest

The authors declare that they have no known competing financial interests or personal relationships that could have appeared to influence the work reported in this paper.

Acknowledgements

We acknowledge Frédéric Danoix for providing us with the material for the study. The ANR is thanked for funding through the project ANR-22-CE08-0016-01. Region Normandie and FEDER are thanked for their support in the framework of project RIN Fusion SATMET. This work was supported by the European Regional Development Fund (ERDF) through the HYDROMEB and SAT UP project. The fracture toughness characterization work was carried out under the GENESIS experimental platform. GENESIS is supported by the Région Haute-Normandie, the Métropole Rouen Normandie, the CNRS via LABEX EMC, and the French National Research Agency as a part of the program "Investissements d'avenir" with the reference ANR-11-EQPX-0020.

Supplementary materials

Supplementary material associated with this article can be found, in the online version, at doi:10.1016/j.scriptamat.2024.116247.

References

[1] L. Norström, The relation between microstructure and yield strength in tempered low-carbon lath martensite with 5% nickel, Metal Sci. 10 (1976) 429–436, https://doi.org/10.1179/030634576790431868.
[2] A. Deschamps, Y. Brechet, Influence of predeformation and ageing of an Al-Zn-Mg Alloy-II. Modeling of precipitation kinetics and yield stress, Acta Mater. 47 (1998) 293–305, https://doi.org/10.1016/S1359-6454(98)00296-1.
[3] J.F. Nie, B.C. Muddle, Microstructural Design of High-Strength Aluminum Alloys, 1998.
[4] X.H. Zeng, P. Xue, L.H. Wu, D.R. Ni, B.L. Xiao, Z.Y. Ma, Achieving an ultra-high strength in a low alloyed Al alloy via a special structural design, Mater. Sci. Eng.: A 755 (2019) 28–36, https://doi.org/10.1016/j.msea.2019.03.126.
[5] K. Edalati, A. Bachmaier, V.A. Beloshenko, Y. Beygelzimer, V.D. Blank, W.J. Botta, K. Bryła, J. Čížek, S. Divinski, N.A. Enikeev, Y. Estrin, G. Faraji, R.B. Figueiredo, M. Fuji, T. Furuta, T. Grosdidier, J. Gubicza, A. Hohenwarter, Z. Horita, J. Huot, Y. Ikoma, M. Janeček, M. Kawasaki, P. Král, S. Kuramoto, T.G. Langdon, D. R. Leiva, V.I. Levitas, A. Mazilkin, M. Mito, H. Miyamoto, T. Nishizaki, R. Pippan, V.V. Popov, E.N. Popova, G. Purcek, O. Renk, Á. Révész, X. Sauvage, V. Sklenicka, W. Skrotzki, B.B. Straumal, S. Suwas, L.S. Toth, N. Tsuji, R.Z. Valiev, G. Wilde, M. J. Zehetbauer, X. Zhu, Nanomaterials by severe plastic deformation: review of historical developments and recent advances, Mater. Res. Lett. 10 (2022) 163–256, https://doi.org/10.1080/21663831.2022.2029779.
[6] A. Mohammadi, N.A. Enikeev, M.Y. Murashkin, M. Arita, K. Edalati, Developing age-hardenable Al-Zr alloy by ultra-severe plastic deformation: significance of supersaturation, segregation and precipitation on hardening and electrical conductivity, Acta Mater. 203 (2021), https://doi.org/10.1016/j.actamat.2020.116503.
[7] A. Deschamps, F. De Geuser, Z. Horita, S. Lee, G. Renou, Precipitation kinetics in a severely plastically deformed 7075 aluminium alloy, Acta Mater. 66 (2014) 105–117, https://doi.org/10.1016/j.actamat.2013.11.071.
[8] V.M. Lopez-Hirata, O. Soriano-Vargas, H.J. Rosales-Dorantes, M.L.S. Muñoz, Phase decomposition in an Fe-40 at.% Cr alloy after isothermal aging and its effect on hardening, Mater. Charact. 62 (2011) 789–792, https://doi.org/10.1016/j.matchar.2011.05.012.
[9] M. Kato, Hardening by spinodally modulated structure in b.c.c. alloys, Acta Metall. 29 (1981) 79–87.
[10] X. Zhou, R. Darvishi Kamachali, B.L. Boyce, B.G. Clark, D. Raabe, G.B. Thompson, Spinodal Decomposition in Nanocrystalline Alloys, Acta Mater. 215 (2021), https://doi.org/10.1016/j.actamat.2021.117054.
[11] W. Xu, Y. Zhong, X. Li, K. Lu, Stabilizing supersaturation with extreme grain refinement in spinodal aluminum alloys, Adv. Mater. (2023) 2303650, https://doi.org/10.1002/ADMA.202303650.
[12] A. Dahlström, Influence of a Mechanical Load On the Ageing of Fe-Cr alloys, Normandie Université, 2019. https://theses.hal.science/tel-02316065. accessed June 22, 2023.
[13] J. Zhou, J. Odqvist, M. Thuvander, P. Hedström, Quantitative evaluation of spinodal decomposition in fe-cr by atom probe tomography and radial distribution function analysis, Microsc. Microanal. 19 (2013) 665–675, https://doi.org/10.1017/S1431927613000470.
[14] H. Zhao, B. Gault, D. Ponge, D. Raabe, F. De Geuser, Parameter free quantitative analysis of atom probe data by correlation functions: application to the precipitation in Al-Zn-Mg-Cu, Scr. Mater. 154 (2018) 106–110, https://doi.org/10.1016/j.scriptamat.2018.05.024.
[15] L. Couturier, F. De Geuser, A. Deschamps, Direct comparison of Fe-Cr unmixing characterization by atom probe tomography and small angle scattering, Mater. Charact. 121 (2016) 61–67, https://doi.org/10.1016/j.matchar.2016.09.028.
[16] J. Duan, H. Wen, C. Zhou, X. He, R. Islamgaliev, R. Valiev, Annealing behavior in a high-pressure torsion-processed Fe–9Cr steel, J. Mater. Sci. 55 (2020) 7958–7968, https://doi.org/10.1007/s10853-020-04560-3.
[17] M. El-Tahawy, Y. Huang, T. Um, H. Choe, J.L. Lábár, T.G. Langdon, J. Gubicza, Stored energy in ultrafine-grained 316L stainless steel processed by high-pressure torsion, J. Mater. Res. Technol. 6 (2017) 339–347, https://doi.org/10.1016/J.JMRT.2017.05.001.
[18] and S.B. J.O. Andersson, T. Helander, L. Höglund, P.F. Shi, Thermo-Calc and DICTRA, Computational tools for materials science CALPHAD. 26 (2002) 273–312.
[19] J. Zhou, J. Odqvist, A. Ruban, M. Thuvander, W. Xiong, J. Ågren, G.B. Olson, P. Hedström, Effect of solution treatment on spinodal decomposition during aging

of an Fe-46.5 at.% Cr alloy, J. Mater. Sci. 52 (2017) 326–335, https://doi.org/10.1007/s10853-016-0333-6.
[20] J.E. Westraadt, E.J. Olivier, J.H. Neethling, P. Hedström, J. Odqvist, X. Xu, A. Steuwer, A high-resolution analytical scanning transmission electron microscopy study of the early stages of spinodal decomposition in binary Fe-Cr, Mater. Charact. 109 (2015) 216–221, https://doi.org/10.1016/j.matchar.2015.10.001.
[21] V. Vojtech, M. Charilaou, A. Kovács, A. Firlus, S.S.A. Gerstl, R.E. Dunin-Borkowski, J.F. Löffler, R.E. Schäublin, Macroscopic magnetic hardening due to nanoscale spinodal decomposition in Fe–Cr, Acta Mater. 240 (2022), https://doi.org/10.1016/j.actamat.2022.118265.
[22] J.W. Cahn, J.E. Hilliard, Free energy of a nonuniform system. I. Interfacial free energy, J. Chem. Phys. 28 (1958) 258–267, https://doi.org/10.1063/1.1744102.
[23] W. Lefebvre, N.V. Skiba, F. Chabanais, M.Y. Gutkin, L. Rigutti, M.Y. Murashkin, T. S. Orlova, Vacancy release upon heating of an ultrafine grain Al-Zr alloy: in-situ observations and theoretical modeling, J. Alloys. Compd. 862 (2021), https://doi.org/10.1016/j.jallcom.2020.158455.
[24] D. Setman, E. Schafler, E. Korznikova, M.J. Zehetbauer, The presence and nature of vacancy type defects in nanometals detained by severe plastic deformation, Materials Sci. Eng.: A 493 (2008) 116–122, https://doi.org/10.1016/j.msea.2007.06.093.
[25] W. Lechner, W. Puff, B. Mingler, M.J. Zehetbauer, R. Würschum, Microstructure and vacancy-type defects in high-pressure torsion deformed Al-Cu-Mg-Mn alloy, Scr. Mater. 61 (2009) 383–386, https://doi.org/10.1016/j.scriptamat.2009.04.027.
[26] M. Zehetbauer, G. Steiner, E. Schafler, A.V. Korznikov, E. Korznikova, Deformation Induced Vacancies with Severe Plastic Deformation: measurements and Modelling, Materials Science Forum 503-504 (2006) 57–64, https://doi.org/10.4028/www.scientific.net/msf.503-504.57.
[27] S. Chakravarty, M. Jiang, U. Tietze, D. Lott, T. Geue, J. Stahn, H. Schmidt, Migration and annihilation of non-equilibrium point defects in sputter deposited nanocrystalline alpha-Fe films, Acta Mater. 59 (2011) 5568–5573, https://doi.org/10.1016/j.actamat.2011.05.029.
[28] A. Seeger, Lattice Vacancies in High-Purity a-Iron, Phys. Stat. Sol. (a) 167 (1998) 289–311.
[29] M.I. Mendelev, Y. Mishin, Molecular dynamics study of self-diffusion in bcc Fe, (n.d.). https://doi.org/10.1103/PhysRevB.80.144111.
[30] E. Del Rio, J.M. Sampedro, H. Dogo, M.J. Caturla, M. Caro, A. Caro, J.M. Perlado, Formation energy of vacancies in FeCr alloys: dependence on Cr concentration, (2011). https://doi.org/10.1016/j.jnucmat.2010.10.021.
[31] W. Puff, X. Zhou, B. Oberdorfer, B. Scherwitzl, P. Parz, W. Sprengel, R. Würschum, Comprehensive defect characterization of different iron samples after severe plastic deformation. J Phys Conf Ser, Institute of Physics Publishing, 2013, https://doi.org/10.1088/1742-6596/443/1/012033.
[32] J.A. Muñoz, O.F. Higuera, A.H. Expósito, A. Boulaajaj, R.E. Bolmaro, F.D. Dumitru, P.R. Calvillo, A.M. Jorge, J.M. Cabrera, Thermal stability of ARMCO iron processed by ECAP, Int. J. Adv. Manuf. Technol. 98 (2018) 2917–2932, https://doi.org/10.1007/s00170-018-2353-7.
[33] S.K. Sarkar, P. Maheshwari, P.K. Pujari, A. Biswas, Co-evolution of point defects and Cr-rich nano-phase in binary Fe-20 at.% Cr alloy: a comprehensive investigation using positron annihilation spectroscopy and atom probe tomography, Acta Mater. 268 (2024) 119740, https://doi.org/10.1016/J.ACTAMAT.2024.119740.
[34] H.C. Akuezue, J. Stringer, Interdiffusion in ternary Fe-Cr-AI alloys, Metallur. Trans. A 20 (1989) 2767–2781, https://doi.org/10.1007/BF02670169/METRICS.
[35] D.N. Demidov, E.A. Smirnov, Effect of Irradiation on Interdiffusion in Fe–Cr System, Inorganic Mater.: Appl. Res. 10 (2019) 525–528, https://doi.org/10.1134/S2075113319030080.
[36] D. Mukherjee, A. Forslund, L. Höglund, A. Ruban, H. Larsson, J. Odqvist, Towards predictive simulations of spinodal decomposition in Fe-Cr alloys, Comput. Mater. Sci. 202 (2022), https://doi.org/10.1016/j.commatsci.2021.110955.
[37] D. Tabor, The physical meaning of indentation and scratch hardness, Br. J. Appl. Phys. 7 (1956) 159, https://doi.org/10.1088/0508-3443/7/5/301.
[38] A. Hohenwarter, R. Pippan, Anisotropic fracture behavior of ultrafine-grained iron, Materials Sci. Eng.: A 527 (2010) 2649–2656, https://doi.org/10.1016/J.MSEA.2009.12.033.
[39] A. Hohenwarter, C. Kammerhofer, R. Pippan, The ductile to brittle transition of ultrafine-grained Armco iron: an experimental study, J. Mater. Sci. 45 (2010) 4805–4812, https://doi.org/10.1007/S10853-010-4635-9/FIGURES/7.
[40] I. Issa, A. Hohenwarter, R. Fritz, D. Kiener, Fracture properties of ultrafine grain chromium correlated to single dislocation processes at room temperature, (n.d.). https://doi.org/10.1557/jmr.2019.140.
[41] Y.C. Hsieh, L. Zhang, T.F. Chung, Y.T. Tsai, J.R. Yang, T. Ohmura, T. Suzuki, In-situ transmission electron microscopy investigation of the deformation behavior of spinodal nanostructured δ-ferrite in a duplex stainless steel, Scr. Mater. 125 (2016) 44–48, https://doi.org/10.1016/j.scriptamat.2016.06.047.
[42] T. Suzudo, H. Takamizawa, Y. Nishiyama, A. Caro, T. Toyama, Y. Nagai, Atomistic modeling of hardening in spinodally-decomposed Fe–Cr binary alloys, Journal of Nuclear Materials 540 (2020) 152306, https://doi.org/10.1016/J.JNUCMAT.2020.152306.
[43] T. Xin, Y. Zhao, R. Mahjoub, J. Jiang, A. Yadav, K. Nomoto, R. Niu, S. Tang, F. Ji, Z. Quadir, D. Miskovic, J. Daniels, W. Xu, X. Liao, L.-Q. Chen, K. Hagihara, X. Li, S. Ringer, M. Ferry, Ultrahigh specific strength in a magnesium alloy strengthened by spinodal decomposition, Sci. Adv 7 (2021). https://www.science.org.
[44] V.M. Lopez-Hirata, E.O. Avila-Davila, M.L. Saucedo-Muñoz, J.D. Villegas-Cardenas, O. Soriano-Vargas, Analysis of Spinodal Decomposition in Al-Zn and Al-Zn-Cu Alloys Using the Nonlinear Cahn-Hilliard Equation, Materials Research 20 (2017) 639–645, https://doi.org/10.1590/1980-5373-MR-2015-0373.
[45] B. Sankar, C. Vinay, J. Vishnu, K.V. Shankar, G.P. Gokul Krishna, V. Govind, A. J. Jayakrishna, Focused Review on Cu–Ni–Sn Spinodal Alloys: from Casting to Additive Manufacturing, Met. Mater. Int. 5 (29) (2022) 1203–1228, https://doi.org/10.1007/S12540-022-01305-6, 2022 29.